# Dalton Transactions

Accepted Manuscript






ROYAL SOCIETY OF CHEMISTRY

www.rsc.org/dalton

Dalton Transactions

ARTICLE

# Introduction of $CoCl_2 \cdot 6H_2O$ into $Co_3O_4$ for Enhancement of Hydroxyl Radicals and Effective Charges Separation

Received 00th January 20xx,
Accepted 00th January 20xx

DOI: 10.1039/x0xx00000x

www.rsc.org/

Ying-juan Hao, Fa-tang Li*, Jun Zhao, Rui-hong Liu, Xiao-jing Wang, Yu-pei Li and Ying Liu

Porous sphere-like tricobalt tetraoxide ($Co_3O_4$)-cobalt chloride hydrate ($CoCl_2 \cdot 6H_2O$, CCH) heterojunctions are obtained by a one-step facile solution combustion route. The heterostructure is confirmed by XRD, HRTEM, and XPS measurements. Their photocatalytic performances are evaluated by the degradation of methyl orange (MO) and the reduction removal of Cr(VI) ion under visible light irradiation. The heterojunction containing 81.5wt% $Co_3O_4$ and 18.5wt% CCH exhibits the highest photocatalytic performance, of which the pseudo-first-order reaction rate constant is 10.0 and 8.7 times that of pure $Co_3O_4$ towards MO degradation and Cr(VI) reduction, respectively. This enhancement in activity can be attributed to the effective electron transfer from the conduction band of $Co_3O_4$ to that of CCH, which is verified with a double increase of photocurrent valve of the heterjunction sample electrode in comparison with bare $Co_3O_4$ sample electrode. Electron paramagnetic resonance, fluorescence spectrophotometer and scavenger experiments indicate that photo-induced holes, hydroxyl and superoxide anion radicals are the active species responsible for the photo-oxidation of MO. The reasons for the formation of theses species are discussed and proposed based on the band gap structures of $Co_3O_4$ and CCH. The recycle experiment results indicate that the activity can be regained by remedial experiment.

## 1. Introduction

An increasing serious pollution from wastewater would have a potential harm to environment and human health. Therefore, how to eliminate toxic organic and inorganic pollutants in wastewater is a current imperative need to human beings and society. Compared with traditional processing methods, photocatalysis is an effective strategy in degrading the abovementioned pollutants because of its high efficiency, cleanness and nontoxicity.[1–5] In the past decades, titanium dioxide has been extensively investigated and applied; however, its wide band gap of 3.2 eV inhibits the practical application.[1,2] To improve the utilization efficiency of sunlight, many researchers have devoted to the development of novel photocatalysts with narrow band gaps, such as g-$C_3N_4$,[3] bismuth-based [4,5] and silver-based materials.[6]

As a typical multifunction semiconductor, $Co_3O_4$ is usually applied in the fields of magnetics,[7] electrochemistry [7,8] and catalysis.[9] In addition, $Co_3O_4$ is also demonstrated to be a photocatalyst. [10,11] Nevertheless, the photocatalytic property of $Co_3O_4$ is unsatisfactory because of the high recombination rate of photo-induced electron-hole pairs. To further improve its photocatalytic activity, some approaches have been employed, including controlling particle size [12] or morphology,[10,13] doping with non-metal or metal elements, such as F [14] and Mg, Ni or Mn,[15,16] or loading $Co_3O_4$ on various supports for the improvement of the dispersion of $Co_3O_4$.[17–21] Besides the aforementioned strategies, constructing heterojunctions is another effective method to inhibit photo-induced carriers' recombination, hence improving photocatalytic performance.[22–24] To date, most $Co_3O_4$-based heterojunctions are obtained by multi-step methods such as co-impregnation,[24] impregnation,[25] and flame spray pyrolysis.[26] However, their limited contact area and/or weak interfacial interaction of heterojunction interface are not conductive to an effective transfer of photo-induced carriers. Because of the different growth mechanisms and reaction rates of different material, engineering complex hybrid photocatalysts via on-pot preparation is still a challenging but exciting topic. [27]

Solution combustion synthesis (SCS) is a time- and energy-efficiency technique.[28,29] Furthermore, in constructing hybrids, SCS can assure high homogeneity of objective composites because of the aqueous starting materials, which endows the heterojunctions with more active contact sites, thus enhancing separation efficiency of photo-induced charges.[29] Our group have developed bismuth oxyhalide- and $Fe_2O_3$-based composites, which exhibited their superior photocatalytic performance.[30–32] According to our research results, we have proposed that the diethylamine hydrochloride (DH) ($(C_2H_5)_2N \bullet HCl$) can act as an reactant supplying chlorine element besides the role of fuel. For $Co_3O_4$, if DH was introduced to synthesize $Co_3O_4$, whether could a cobalt chloride/$Co_3O_4$ composite be eventually obtained?

Therefore, the band gap potentials of bare $Co_3O_4$ and bare cobalt chloride hydrate ($CoCl_2 \cdot 6H_2O$, CCH) were first investigated before designing this composite. We found that the band gaps of these two components match well each other. It suggests that there is

*College of Science, Hebei University of Science and Technology, Shijiazhuang 050018, China. Email: lifatang@126.com.*

theoretically a possibility for the presence of the heterojunction between $Co_3O_4$ and CCH. In my opinion, there are two main advantages for the presence of CCH compared with other compounds containing no crystal water: (1) appropriate band structure matching, which conduction band can accept photo-induced electrons from that of $Co_3O_4$; (2) the crystallization water in CCH can in-situ contact and then react with photo-generated holes of $Co_3O_4$ to form hydroxyl radicals. In this work, porous sphere-like $Co_3O_4$-CCH heterojunctions are successfully obtained with DH as a chlorine source and simultaneously as fuel. The photocatalytic performances of the obtained heterojunctions are evaluated by the removal of hexavalent chromium (Cr(VI)) and methyl orange (MO). This work would not only offer a reference for constructing $Co_3O_4$-based hybrids with a facile combustion route, but also provide a new design idea for exploring a highly efficient heterojunction in enhancing the generation of hydroxyl radicals.

## 2. Experimental

### 2.1 Preparation of catalysts

All chemicals appeared in this work were purchased from Aladdin (Shanghai, China) and used as received without further purification. In a typical synthesis process, various amount of DH (0~0.0060 mol)), 0.01 mol of cobalt nitrate hexahydrate ($(Co(NO_3)_2{\cdot}6H_2O)$) and 0.015 mol of urea ($CN_2H_4O$) were mixed. The mixtures were continually heated on an electric furnace until the combustion of the solution was finished. The black products were denoted and listed in Table 1.

### 2.2 Characterizations

X-ray diffraction (XRD) patterns were acquired on Rigaku D/MAX 2500 X-ray diffractometer using Cu-Kα radiation. Fourier transform infrared (FTIR) spectra were obtained on a Shimadzu IR-Prestige 21 spectrometer with pressing potassium bromide troche. The special surface areas ($S_{BET}$) and porous structure were received on Micromeritics Tristar 2020 adsorption instrument. The $S_{BET}$ values were calculated using Brunauer, Emmett and Teller (BET) method. Scanning electron microscopy (SEM) were performed on JEOL JSM-7500 electron microscope. Transmission electron microscopy (TEM) and high resolution electron microscopy (HRTEM) images were accomplished on a JEOL JEM-2010 electron microscopy. The X-ray photoelectron spectroscopy (XPS) spectra were obtained on a PHI 1600 ESCA XPS system. The zeta-potential performance of S3 sample was characterized by HORIBA SZ-100-Z Nanoparticle Analyzer. Photoelectrochemical measurements were performed on an electrochemical workstation (CHI-660E, China) using a conventional three-electrode quartzcells. The electrolyte used in this work was a mixture of 0.2 M $Na_2S$ and 0.04 M $Na_2SO_3$ solution. The as-obtained photocatalyst film electrodes deposited on a cleaned fluoride-tin oxide glass as the working electrode.

### 2.3 Photocatalytic activity tests

Photocatalytic MO degradation was performed under a 350 W Xe-lamp irradiation with a 420 nm optical filter as a visible light source. The light intensity of the lamp was 0.16 kW/m$^2$ at 420 nm, which was measured by a light-intensity meter. In a typical evaluation process, 0.10 g of catalyst was added to 100 mL MO (10 mg/L) aqueous solution. At given time intervals, 3 mL of the suspension was sampled, centrifuged and filtered to remove the photocatalyst. To ensure the adsorption/desorption equilibrium, the suspensions were stirred continuously in dark for 30 min before irradiation. The MO decoloration rate was reported as $C/C_0$, where $C_0$ and C were the concentrations of 10 mg/L and after photocatalysis, respectively. The concentration of MO was tested by spectroscopic analysis at 464 nm.

**Table 1.** Phase composition, particle size and the BET results of the obtained samples.

| Sample | Co/DH (molar ratio) | Phase composition/% | | $S_{BET}$/ m$^2$/g | Pore volume/ cm$^3$/g | Average pore diameter / nm |
|---|---|---|---|---|---|---|
| | | $Co_3O_4$ | CCH | | | |
| S1 | 1: 1.5: 0 | 100 | 0 | 8.7 | 0.025 | 11.0 |
| S2 | 1:1.5:0.50 | 95.1 | 4.9 | 4.3 | 0.033 | 30.9 |
| S3 | 1: 1.5:0.55 | 81.5 | 18.5 | 6.9 | 0.034 | 17.9 |
| S4 | 1: 1.5:0.60 | 67.6 | 32.4 | 3.4 | 0.028 | 30.6 |

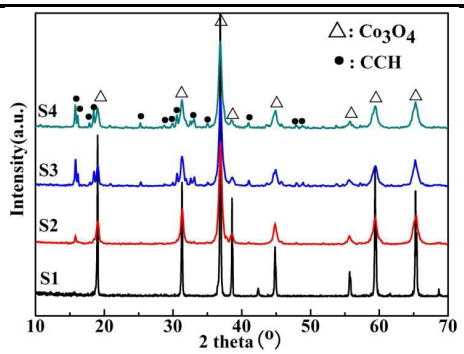


**Fig. 1.** XRD patterns of the obtained samples.

Photocatalytic reduction of Cr(VI) ions was determined colorimetrically at 543 nm using the diphenylcarbazide (DPC) method.[33] After adsorption and irradiation, the suspension was collected and centrifuged. 1mL of sample was mixed with 9 mL $H_2SO_4$ (0.2 mol/L ) and 0.2 mL of freshly prepared 0.25% DPC in acetone (w/v) in a 25 mL beaker. The concentration was determined by spectroscopic analysis at 543 nm. The Cr(VI) removal efficiency was reported as $C/C_0$, where $C_o$ and C were the Cr(VI) concentrations of 50 mg/L and after photocatalysis, respectively.

### 2.4 Reactive species determination

In order to determine the main active species in the system, 1,4-benzoquinone (BQ),[34] isopropanol (IPO)[30] and ammonium oxalate (AO)[35] were introduced into the solution of MO, respectively. The presence and role of hydroxyl radicals (·OH) using 2-hydroxyterephthalic (2-HTA) as a probe was confirmed on a Hitachi F-4600 fluorescence spectrophotometer (excitation wavelength at 315 nm). To observe fluorescence spectra, 0.10 g of catalyst was added to 100 mL terephthalic acid (TA) (0.5 mM) aqueous solution and the mixture was irradiated under visible light. At every 20 minutes (min) intervals, 3 mL of the suspension was sampled, centrifuged and measured on the fluorescence spectrophotometer. The generation of superoxide anion radicals ($\cdot O_2^-$) were carried on a Bruker EMX-8/2.7 X-band electron paramagnetic resonance (EPR) under visible light irradiation, which can react with 5,5-dimethyl-L-pyrroline-N-oxide (DMPO) to produce an adduct with a representative EPR signals.

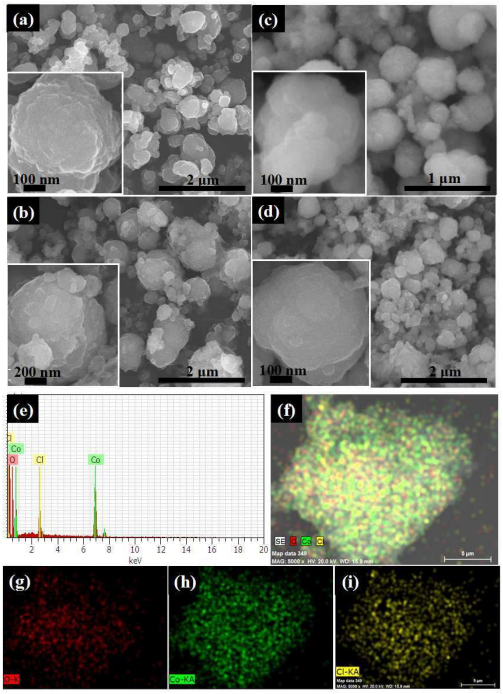


**Fig. 2.** Typical SEM images of the obtained samples: (a) S1; (b) S2; (c) S3; (d) S4. Left insets are high-magnification SEM images of the selected particles to display structure in detail; (e) EDS image of a selected particle in (c); (f-i) EDS mapping results from the aforementioned particle in (c).

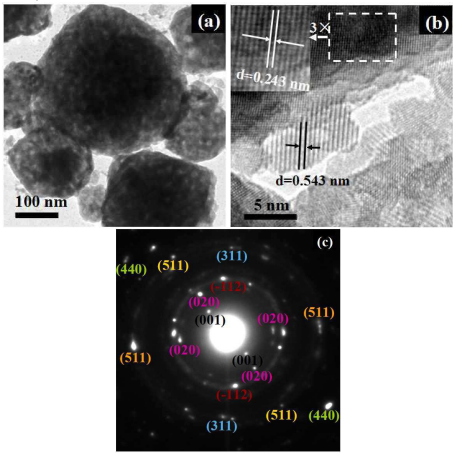


**Fig. 3.** (a) TEM, (b) HRTEM and (c) SAED images of sample S3.

## 3. Results and discussion

### 3.1 Characterization of the samples

Fig. 1 shows the XRD patterns of the samples. It can be seen that when only urea was employed as fuel, the characteristic diffraction peaks of the sample S1 arising from 19.03°, 31.32°, 36.90°, 44.88°, 59.45° and 65.34° are attributed to (111), (220), (311), (400), (511) and (440) planes of cubic $Co_3O_4$ phase (JCPDS 076-1802),[36,37] indicating its pure $Co_3O_4$ phase. When DH was introduced besides urea, many new diffraction peaks at 15.76°, 16.09°, 17.82°, 18.44°, 25.25°, 30.54°, 32.53°, 37.39°, 40.98°, 45.80° and 47.92° are also detected on S2, S3 and S4 samples, which are assigned to (001), (110), (-201), (-111), (020), (-112), (220), (-222), (400), (-512) and (-132) planes of monoclinic CCH (JCPDS 080-1559) phase. These peaks verify the coexistence of $Co_3O_4$ and CCH in these samples. The phase compositions of the obtained samples are calculated by the RIR method[31] and listed in Table 1. When only urea is used as fuel, the formation of pure $Co_3O_4$ is put forward in equation (1):

$$12Co(NO_3)_2{\cdot}6H_2O+18CO(NH_2)_2 \rightarrow 4Co_3O_4+18CO_2+30N_2+O_2+108H_2O \quad (1)$$

In the presence of $(C_2H_5)_2NH{\cdot}HCl$), CCH is formed according to the following equation (2) :

$$Co(NO_3)_2{\cdot}6H_2O+2(C_2H_5)_2{\cdot}NH{\cdot}HCl+7O_2 \rightarrow CoCl_2{\cdot}6H_2O+12H_2O+8CO+2N_2 \quad (2)$$

Typical morphologies of the obtained samples are indicated in Fig. 2. Comparison among the images reveals the formation process of sphere-like particles. Fig. 2a displays that bare $Co_3O_4$ particles are in shape of flake and its surface looks smooth. Increasing the DH amount, many new CCH particles appear on the surface of $Co_3O_4$ (see Fig. 2b), making the surface become fairly rough and then the particle dimensions begin to grow. Fig. 2c indicates that some sphere-like particles are formed when the DH amount is 0.55 mol. However, it can be seen that the sphere-like morphology is destroyed and its surface begins to become denser when DH amount is increased to 0.60 mol (shown in Fig. 2d). Obviously, insets of Fig. 2 by every close-up view of the selected particles reveal this morphology change resulted from different amount addition of DH. The element composition of sample S3 is analyzed by EDS analysis (Fig. 2e). The element mapping results (Fig. 2f-2i) indicate that an uniform distribution of cobalt, oxygen and chlorine elements is distinctly observed on the selected particle, which is in reasonable agreement with the EDS image displayed in Fig. 2e.

The formation of porous structure of sample S3 is demonstrated by TEM analysis. As shown in Fig. 3a, the sphere-like sample exhibits porous structure. Fig. 3b displays the representative HRTEM pattern of sample S3. The calculated interplanar spacings of 0.243 and 0.562 nm can be assigned to (311) plane of cubic $Co_3O_4$ phase and (001) plane of monoclinic CCH phase, respectively, which is well consistent with the XRD result. Moreover, the interface between $Co_3O_4$ and CCH can be also clearly observed, which suggests that a heterostructure between $Co_3O_4$ and CCH are formed. Right-bottom inset of Fig. 3c displays a typical selected-area electron diffraction (SAED) pattern. The diffraction rings are (001), (020), (-112), (311), (511) and (440) planes, respectively. The first three planes can be attributed to CCH phase, the rest ones to $Co_3O_4$ phase, suggesting that the heterojunction indeed formed.

As shown in Fig. S1a in ESI.†, every sample displays a typical IV isotherm, indicating that the pore structure property is not influenced by the introduction of CCH. Moreover, the similarity of adsorption isotherms illustrates that the obtained samples have similar textures.[38] Their corresponding results of $S_{BET}$, pore volume and average pore size are also listed in Table 1. Table 1 exhibits that no significant regularity of average pore size can be obtained with increasing the DH amount. Fig. S1b in ESI.† indicates that every sample displays a mesoporous and/or macroporous pore size distribution behavior, which is resulted from the gas emission during combustion process.[39]

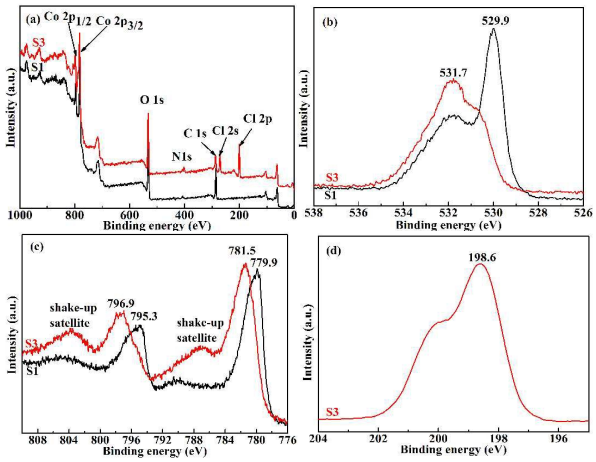


**Fig. 4.** XPS spectra of samples S1 and S3: (a) survey scan; (b) O 1s; (c) Co 2p; (d) Cl 2p.

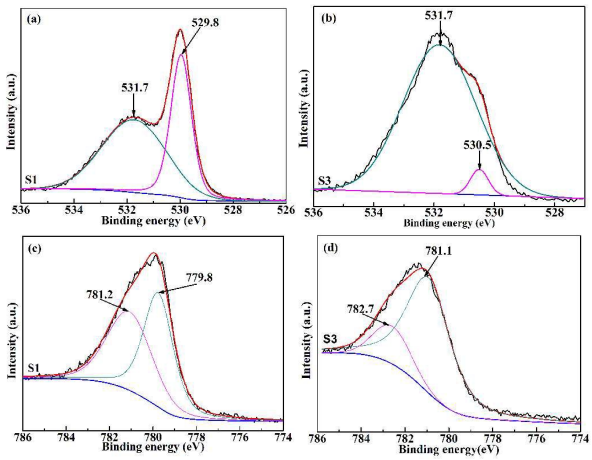


**Fig. 5.** XPS fitted curve of O1s (a and b) and Co 2p3/2 (c and d) in samples S1 and S3.

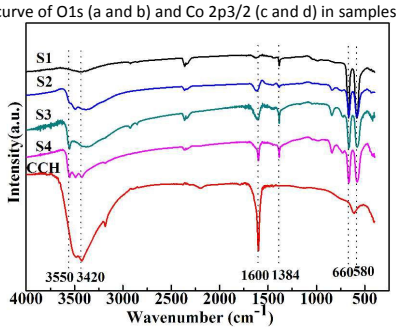


**Fig. 6.** FT-IR spectra of the obtained samples.

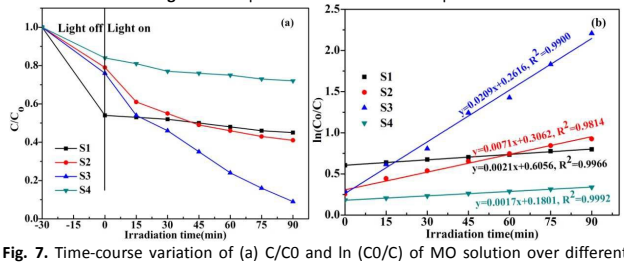


**Fig. 7.** Time-course variation of (a) C/C0 and ln (C0/C) of MO solution over different samples under visible light illumination.

Fig. 4 shows the XPS spectra of samples S1 and S3. As displayed in Fig. 4a, a co-presence of Co, O, N, C and Cl elements in S3 is demonstrated, which is well consistent with the result of SEM-EDS. Two O 1s peaks with different binding energies (BE) appear on the surface of S1 and S3 (see Fig. 4b). From the XPS spectra for Co element (Fig. 4c), two associated shake-up satellite peaks can be observed for S1 besides the split orbit peaks of Co $2p_{1/2}$ and Co $2p_{3/2}$. The presence of satellite peaks shows that the Co element in S1 has different oxidation states,[40] which was in good agreement with the report.[41,42] A similar spectrum of Co 2p is also found for S3. Fig. 4d shows that the Cl $2p_{3/2}$ orbital displays a peak with bind energy at 198.6 eV for S3.[43]

To further investigate the effects of the CCH on the valence state of Co and O elements, the O 1s and Co $2p_{3/2}$ peaks are deconvoluted by Lorentzian-Gaussian method (shown in Fig. 5) for S1 and S3, respectively. For sample S1, the peaks at 530±0.2 eV and 532±0.2 eV (Fig. 5a) are attributed to the lattice oxygen ($O_L$) in cobalt spinel oxide[41,44] and chemisorbed oxygen species ($O_c$) or hydroxyl groups,[18, 40–44] respectively. Herein, the peak at 531.7 eV is assigned to surface hydroxyl groups as $O_c$ species. Obviously, the intensity of $O_c$ species on S3 surface (Fig. 5b) is stronger than that on S1 surface, indicating that the formation of surface $O_c$ on S3 is derived from the presence of crystallization water in CCH. It is demonstrated that more hydroxyl groups have a positive effect on the photocatalytic oxidation property.[18,45] The BE of Co $2p_{2/3}$ peak arising from S1 sample is deconvoluted into two peaks at 779.8 and 781.2 eV (Fig. 5c), which is a characteristic of $Co_3O_4$ phase.[44] When the CCH is introduced, the Co $2p_{2/3}$ peaks of S3 shift to high BE of 781.2 and 782.7 eV (Fig. 5d), respectively. This BE change of Co $2p_{2/3}$ electron should be related with an interaction between $Co_3O_4$ and CCH in the heterojunction.

Fig. 6 displays the FT-IR spectra of the obtained samples. In order to further confirm the presence of surface hydroxyl groups from crystal water, commercial CCH are also characterized by FT-IR method. The peaks at 3490, 3420 and 1600 $cm^{-1}$ are clearly observed in the FT-IR spectra of commercial CCH, which correspond to the asymmetric stretching, symmetric stretching and deformation vibration models of hydroxyl species from crystal water molecular. For bare $Co_3O_4$ sample (S1), there appear some peaks at 1384, 660 and 580 $cm^{-1}$ besides 3420 and 1600 $cm^{-1}$. Herein, the narrow peak at 1384 $cm^{-1}$ belongs to the stretching mode of unburned nitrate ions[46] and the strong peaks at 660 and 580 $cm^{-1}$ are assigned to the spinel structure of $Co_3O_4$ phase.[21,47] By contrast, the peak intensities of $Co_3O_4$ decrease while the peak intensities of hydroxyl species increase. The high content of CCH in the heterojunction is conducive to the formation of surface hydroxyl species from crystal water, which is well consistent with the XPS result.

### 3.2 Potocatalytic performance evaluation

The photocatalytic activities of the obtained samples are evaluated by the degradation of MO and removal of Cr(VI) ions, respectively. Fig. 7 indicates the $C/C_0$ value as the function of irradiation time. As shown in Fig. 7a, the adsorption rate is 46% while the photocatalytic activity is increased only by 10% within 90 min over bare $Co_3O_4$, showing its poor photocatalytic ability. After 90 min of irradiation, the degradation efficiencies of MO over S2, S3 and S4 achieved 59%, 90% and 30%, respectively. Obviously, the sample S3 shows the highest photocatalytic oxidation activity. Because of the low concentration of MO, the photocatalytic reactions should follow the Langmuir-Hinshelwood pseudo-first-order kinetics model.[31] The apparent reaction rate constants of the obtained

samples for MO degradation are calculated on basis of the apparent pseudo-first-order model. It can be seen from Fig. 7b that the apparent reaction rate constant of S3 is 10.0 times as high as that of bare $Co_3O_4$.

Huang and co-workers have reported that the oxidation/reduction reactions would occur due to the presence of $Co^{3+}$ ions in photoelectrochemical catalysis fields.[48] In this work, the photocatalytic reduction behavior of the obtained heterojunction is also investigated with Cr(VI) ion as a pollutant model. Fig. 8a indicates the removal efficiency of 50 mg/L Cr(VI) ions in weak acidic solution (pH 6.0) over the obtained samples. When bare $Co_3O_4$ is irradiated under visible light, it can be initiated and then generated electron-hole pairs on the surface. Because of the presence of $Co^{2+}$ and $Co^{3+}$ ions in bulk phase, the $Co_3O_4$ particle itself can act as an electron or hole collector. When bare $Co_3O_4$ is continually irradiated, there would be two reduction behaviors: (1) the reduction of $Co^{3+}$ to $Co^{2+}$;[49] (2) the Cr (VI) reduction to Cr(III). Because the reduction potential of $Co^{3+}/Co^{2+}$ is more negative than that of $Cr_2O_7^{2-}/Cr^{3+}$, the occurrence of the latter reduction behavior does not actually appear over bare $Co_3O_4$ within 90 min. When the heterojunction was employed in this work, the photocatalytic reduction performance was significantly promoted. Their corresponding removal efficiencies reach 78%, 97% and 74% within 180 min over S2, S3, and S4, respectively. As shown in Fig. 8b, the apparent reaction rate constants for the Cr(VI) reduction removal over S1, S2, S3 and S4 are 0.00192, 0.00512, 0.01688 and 0.0052 min-1, respectively. That is, the apparent reaction rate constant of the S3 sample is 8.7 times that of bare $Co_3O_4$.

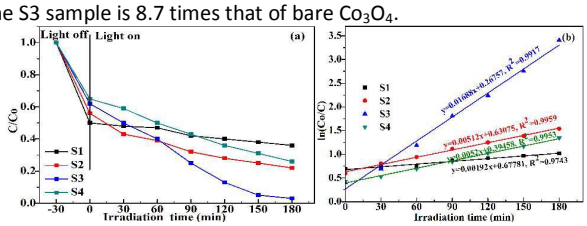


**Fig.8.** Time-course curves of (a) C/Co and ln (Co/C) of Cr(VI) removal in weak acidic solution (pH 6.0) over the obtained samples under visible light illumination.

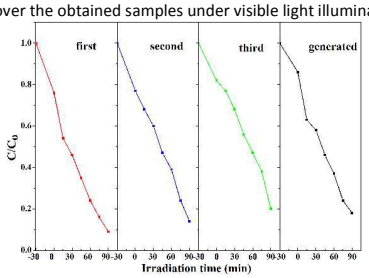


**Fig. 9.** Recycling test of sample S3. Reaction conditions: 0.2 g of catalyst, 200 mL 10 mg/L MO aqueous solution.

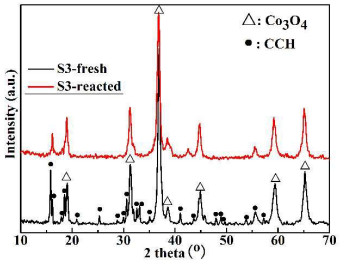


**Fig.10.** XRD patterns of the S3 sample before and after the photocatalytic reaction.

**Table 2** Phase composition of the samples

| sample | Phase composition (%) | |
|---|---|---|
| | $Co_3O_4$ | CCH |
| S3-fresh | 81.5 | 18.5 |
| S3-reacted | 90.2 | 10.8 |

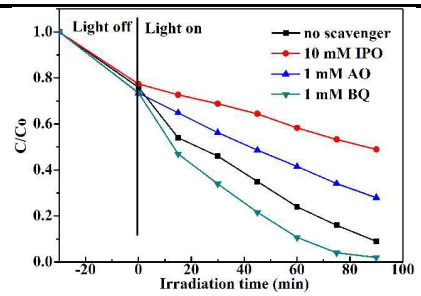


**Fig.11.** Photocatalytic degradation activity of MO over the S3 sample in the presence of different scavengers.

### 3.3 Stability and regeneration of the obtained heterojunction

To investigate the stability of the obtained heterojunction, we did some recycle experiments of S3 for photocatalytic oxidation degradation. The recycle experiment result is shown in Fig. 9. It is found that the photocatalytic performance debases obviously after three cycles. There may be two main reasons for the deactivation: (1) a small amount dissolution of $Co^{2+}$ and/or $Cl^-$ ions;[50,51] (2) some intermediates adsorbed on the surface.[25] In order to clarify the deactivation reasons, we did some remedial experiments and characterized the reacted S3 sample by XRD (Fig. 10), respectively. When the reacted sample was firstly impregnated in 1M CCH aqueous solution and then calcined 473 K in air for 4 h, the debasement of photocatalytic activity could be regenerated. The degradation efficiency of the regenerated sample achieves 82% within 90 minutes. However, we found that MO molecules could not be degraded over bare $Co_3O_4$ in CCH solution under the same degradation conditions, showing the positive effect of CCH existed as solid. Fig. 10 shows that the crystal structure of S3 does not change after the recycle reaction while the relative content of CCH is obviously decreased and that of $Co_3O_4$ is increased (see Table 2). Therefore, it can be inferred that the activity deactivation is mainly concerned with the destruction of the heterojunction because of the CCH dissolution.

### 3.4 Adsorption mechanism

It is clear from Fig. 7 that the samples exhibit excellent adsorptive ability for MO. The adsorption properties of photocatalysts are determined by two main factors: (1) specific surface area and pore structure; (2) surface charge property. Therefore, the $S_{BET}$ of the obtained samples and zeta potential property of the S3 sample are investigated. As shown in Table 1, the influences of $S_{BET}$ on their adsorption quantity can be negligible because all the $S_{BET}$ values are less than 10 $m^2/g$. Seen from Fig. S2 in ESI.†, the point of zero zeta potential of the S3 is at about 9.7. Therefore, anionic pollutant molecules can be easily adsorbed on S3 surface due to an electrostatic attraction at pH<9.7,[52] which is well coincided with the results of adsorption rates for anionic dye MO and Cr(VI) anions at pH=6. Moreover, the adsorption rates were decreased gradually when the CCH content in heterojunctions was increased. It can be inferred that there should appear an electrostatic repulsion

between $Cl^-$ anion (and/or surface hydroxyl groups) and anionic pollutant molecules, as displayed in Fig. 7 and Fig. 8.

### 3.5 Mechanism of charge carriers transfer and photocatalytic degradation

#### 3.5.1 Active species determination

In this work, we have investigated the effects of nitrogen and some scavengers on the photocatalytic oxidation properties for MO dyes molecules over sample S3, respectively. The results are shown in Fig. 11. When nitrogen was pumped in the solution, the decoloration efficiency markedly decreased. It suggests that the photocatalytic performance is related with dissolved oxygen in aqueous solution to some extent. When the aforementioned scavengers (BQ, IPO and AO) were introduced, all the degradation efficiencies were also significantly inhibited. Therefore, it can be drawn a conclusion that $\cdot O_2^-$, ·OH and $h^+$ species are active species for MO degradation in this system.

To further demonstrate the presence of free ·OH active radicals generated in the solution and its influence on the oxidative degradation activity, the ·OH radicals are detected by a photoluminescence (PL) technique using 2-HTA as probe. The higher emission peak intensity of 2-HTA is, the more ·OH radicals in solution are. The PL results are revealed in Fig. 12. There are two emission peaks at about 355 and 400 nm for S1 and S3 during visible light illumination (as shown in Fig.12 a-b). The peak at 355 nm is described to the Raman peak of water. The peak at 400 nm is assigned to the emission peak of 2-HTA molecules. The blue shift from 420 nm to 400 nm is related with the bonding interaction between small amount dissolution of $Co^{2+}$ ion and 2-HTA molecule. As indicated in Fig. 12c, the ranking of the fluorescence intensity of 2-HTA on different samples are in the order of S3>S2>S4>S1, which indicates that the presence of CCH is conducive to the formation of ·OH radicals because the crystalline water in CCH can easily combine with photo-generated holes of $Co_3O_4$ to form ·OH radicals. In addition, 2-HTA can be generated via the reaction of $h^+$ and TA. [53] To detect whether there are hydroxyl radicals or not, a supplementary PL test was carried out over S3 by adding scavengers including AO ($h^+$ scavenger, 1 mM), IPO (·OH scavenger, 10 mM), and dimethyl sulfoxide (as ·OH scavenger, 1 mM DMSO),[53] into the TA solution. It is seen from Fig. 12d. that both the scavengers of $h^+$ and ·OH species can reduce the PL intensity of 2-HTA at 80 min to some extent, suggesting that $h^+$ and ·OH radicals are indeed formed over S3. It also confirmed that TA can be oxidized by $h^+$ species to obtain 2-HTA, which is well agreement with the reference.[53]

In order to further confirm the formation of $\cdot O_2^-$ during the degradation process, trace amounts of DMPO was used to capture $\cdot O_2^-$ by producing a paramagnetic adduct by ESR characterization. As indicated in Fig.13, there appear the characteristics ESR signals of DMPO-·$O_2^-$ adduct over sample S3 under visible light irradiation at various times. Moreover, the intensities of DMPO-·$O_2^-$ adduct signals gradually increase as prolonging the irradiation time from 4 to 12 min. It verifies that the generation of $\cdot O_2^-$ species indeed occurred during the photocatalytic degradation for MO molecules, which is also consistent with the scavenger result. The reason for the occurrence of $\cdot O_2^-$ species will be discussed in the following section.

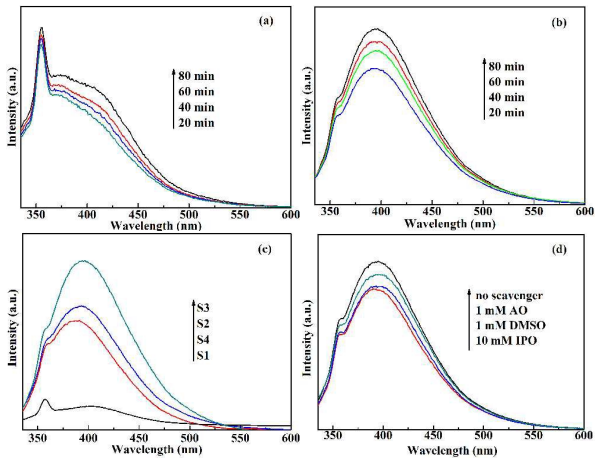


**Fig.12.** ·OH-trapping fluorescence spectra of as-prepared samples in a TA solution (315 nm excitation wavelength): (a) bare Co3O4; (b) S3 sample;(c) different samples at 80 min illumination; (d) the 2-HTA formation over sample S3 in the presence of various scavengers.

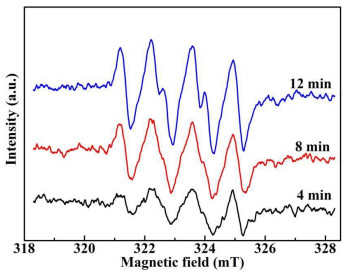


**Fig. 13.** ESR signals of DMPO-·$O_2^-$ adduct over sample S3 under visible light irradiation at different times.

**Table 3** Electronegativity, the calculated energy levels of ECB and EVB for $Co_3O_4$ and CCH.

| samples | electronegativity (X) | estimated energy band gap $E_g$(eV) | calculated $E_{CB}$ (eV) | calculated $E_{VB}$ (eV) |
|---|---|---|---|---|
| $Co_3O_4$ | 5.70[a]/5.903[b] | 2.07[a,b] | 0.2[a]/0.37[b] | 2.27[a]/2.44[b] |
| CCH | 6.95[a] | 3.8[a] | 0.55[a] | 4.35[a] |

[a]estimated from our work, [b]from reference [25]

#### 3.5.2 Photo-induced carriers transfer route and the photocatalytic mechanism

The band gap potentials of bare $Co_3O_4$ and bare CCH are investigated in order to further confirm the presence of the heterostructure. Long et al. [25] have thought that there are two methods to determine the band potential edge: (1) experiment methods on the basis of electrochemical and UV-Vis diffraction reflectance spectra; (2) calculation methods such as the first principle or the atom's Mulliken electronegativity formula. The aforementioned experiment methods do not work due to the optical absorption of black $Co_3O_4$ and the hygroscopicity of CCH. Therefore, their corresponding edge potentials of conduction band ($E_{CB}$) and valence band ($E_{VB}$) are respectively calculated by Mulliken electronegativity formula as follows [31]:

$$E_{VB}=\chi - Ec + 0.5Eg \quad (1)$$

$$E_{CB}=E_{VB}-Eg \quad (2)$$

herein, χ, Eg and Ec are the electronegativity, band gap energy and the energy of free electrons on the hydrogen scale (about 4.5 eV), respectively. The calculation results in this work and reference [25] are listed in Table 3.

According to the band edge positions, the energy band schematic is depicted in Scheme 1. When bare $Co_3O_4$ is irradiated under visible light irradiation, the electrons are excited and transferred to the CB position of $Co_3O_4$ (+0.2 eV). The photo-induced electrons on the CB of $Co_3O_4$ can migrate to that of CCH (+0.55 eV) because the former $E_{CB}$ potential is more negative than that of the latter one. Thus, the transfer of electrons in the heterojunction interface between $Co_3O_4$ and CCH can occur, which is in favor of improving the separation efficiency. Meanwhile, there would appear more available photo-induced holes involved in oxidation processes in comparison with bare $Co_3O_4$. Because the standard potentials of $\cdot OH/H_2O$ (+2.27 eV)[54] is almost equal to the calculated $E_{VB}$ of the heterojunction (+2.27 eV) in this work, so it is impossible that the photo-induced holes can directly react with adsorbed water. However, they can do with surface hydroxyl groups in presence of CCH considering that it is more positive than that of standard potentials of $\cdot OH/OH^-$ (+1.99 eV).[55] Therefore, both the effective photo-induced holes and the in-situ generated ·OH radicals over the heterojunction can participate in the oxidation degradation of MO molecules, which is conformed in the 3.5.1 section.

Notably, when the heterojunction is irradiated under visible light with λ>420 nm corresponding to 2.95 eV energy, the electrons of $Co_3O_4$ can be excited to form a higher negative potential (-0.68 eV) than that of its own CB (+0.2 eV). Because it was more negative than that of $\cdot O_2^-/O_2$ (-0.28 eV),[54] so the $\cdot O_2^-$ species can be generated in containing-dissolved oxygen aqueous solution, which is verified by ESR characterization. The photocatalytic oxidation mechanism is indicated in Scheme 1.

Scheme 2 indicates the degradation mechanism for Cr(VI) removal over the heterojunction under visible irradiation. When only bare $Co_3O_4$ was employed, the photocatalytic reduction efficiency for Cr(VI) removal was found to be very low. However, the heterojunction displayed an excellent degradation behavior for Cr(VI) removal under visible light irradiation, which is possibly related with its own band gap structure. As mentioned above, when the heterojunction is irradiated under visible light with λ>420 nm, the photo-induced electrons from both the CB (+0.2 eV) and higher potential (-0.68 eV) of $Co_3O_4$ can migrate to the CB (+0.55 eV) of CCH. Thus, there appear more separated electrons for the reduction reaction, which accounts for the improvement of photocatalytic reduction performance for Cr(VI) removal.

Herein, the presence of CCH in the heterojunction plays a main role of rapid electron transfer, hence inhibiting the recombination rate of photo-induced carriers and then producing more available holes or electrons further participated in the redox reaction.

Because the separation efficiency of the samples can be also confirmed by photoelectrochemical measurement, the transient photocurrent responses of S1 and S3 are investigated and the result is displayed in Fig. S3 in ESI.†. Obviously, the photocurrent value of the S3 electrode is twice as high as that of the S1 electrode under visible light irradiation ( λ >420 nm) in an on-and-off cycle mode. Considering that $CoCl_2{\cdot}6H_2O$ cannot be excited under visible light

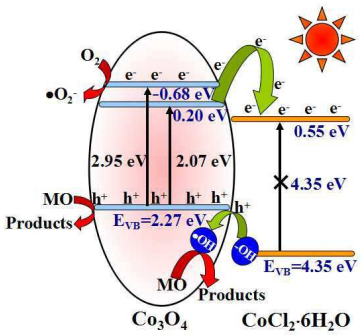


**Scheme 1.** Schematic diagram of photocatalytic oxidation mechanism over the $Co_3O_4/CoCl_2{\cdot}6H_2O$ heterojunction under visible light irradiation (λ>420nm).

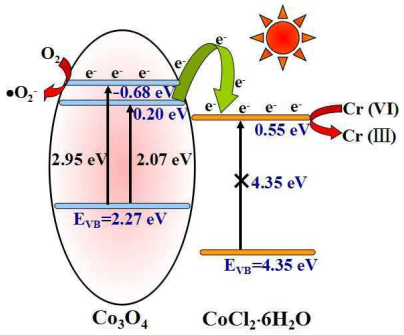


**Scheme 2.** Schematic diagram of photocatalytic reduction mechanism over the $Co_3O_4/CoCl_2{\cdot}6H_2O$ heterojunction under visible light irradiation (λ>420nm).

irradiation due to its wide band gap, the improvement of the photocurrent value is attributed to an effective separation of photo-induced carriers in the presence of the heterojunction interface.

## Conclusions

In summary, a novel porous $Co_3O_4/CoCl_2{\cdot}6H_2O$ heterojunction has been successfully synthesized by one-step solution combustion method. The apparent reaction rate constants of the heterojunction for degradation of MO and removal of Cr(VI) ions are significantly improved than those of bare $Co_3O_4$. The improvements of photocatalytic redox activities over the heterojunction are mainly due to accelerating the transfer of photo-induced electrons and benefiting the formation of ·OH radicals in solution in the presence of $CoCl_2{\cdot}6H_2O$ phase. Although the dissolution of $CoCl_2{\cdot}6H_2O$ would lead to the debasement in activity, the photocatalytic ability can be regained by immersing the used photocatalyst in $CoCl_2{\cdot}6H_2O$ aqueous solution and then calcining it.

## Acknowledgements

We are grateful for the financial support from the National Natural Science Foundation of China (21076060,21376061), the Natural Science Foundation of Hebei Province (B2015208124), the Program for New Century Excellent Talents in University (NCET-12-0686), Scientific Research Foundation for High-Level Talent in University of Hebei Province (GCC2014057), Natural Science Foundation for Distinguished Young Scholar of Hebei Province (B2015208010), and

the Doctoral Science Foundation of Hebei University of Science and Technology (QD201240).

## Notes and references

1 W. K. Jo and T. S. Natarajan, *ACS Appl. Mater. Interfaces*, 2015, **7**, 17138.
2 F. T. Li, X. J. Wang, Y. Zhao, J. X. Liu, Y. J. Hao, R. H. Liu and D. S. Zhao, *Appl. Catal. B: Environ.*, 2014, **144**, 442.
3 X.C. Wang, K. Maeda, A. Thomas, K. Takanabe, G. Xin, J. M. Carlsson, K. Domen and M. Antonietti, *Nat. Mater.*, 2009, **8**, 76.
4 Q. Sun, X. R. Jia, X. F. Wang, H.G. Yu and J. G. Yu, *Dalton Trans.*, 2015, **44**, 14532.
5 H. P. Jiao, X. Yu, Z. Q. Liu, P. Y. Kuang and Y. M. Zhang, *RSC Adv.*, 2015, **5**, 1623.
6 C. L. Yu, G. Li, S. Kumar, K. Yang and R. C. Jin, *Adv. Mater.*, 2014, **26**, 892.
7 X. Wang, W. Tian, T. Y. Zhai, C. Y. Zhi, Y. Bando and D. Golberg, *J. Mater. Chem.*, 2012, **22**, 23310.
8 X. F. Huang, T.C. Cao, M. C. Liu and G. H. Zhao, *J. Phys. Chem.*, C 2013, **117**, 26432.
9 X. W. Xie and W. J. Shen, *Nanoscale*, 2009, **1**, 50.
10 M. Roy, S. Ghosh and M. K. Naskar, *Dalton Trans.*, 2014, **43**, 10248.
11 T. Warang, N. Patel, R. Fernandes, N. Bazzanella and A. Miotello, *Appl. Catal. B: Environ.*, 2013, **132–133**, 204.
12 M. Grzelczak, J. S. Zhang, J. Pfrommer, J. Hartmann, M. Driess, M. Antonietti and X. C. Wang, *ACS Catal.*, 2013, **3**, 383.
13 H. Q. Sun, H. M. Ang, M. O. Tadé and S. B. Wang, *J. Mater. Chem., A*, 2013, **1**, 14427.
14 A. Gasparotto, D. Barreca, D. Bekermann, A. Devi, R. A. Fischer, P. Fornasiero, V. Gombac, O. I. Lebedev, C. Maccato, T. Montini, G. V. Tendeloo and E. Tondello, *J. Am. Chem. Soc.*, 2011, **133**, 19362.
15 J. Rosen, G.S. Hutchings and F. Jiao, *J. Catal.,* 2014, **310**, 2.
16 J. Rosen, G.S. Hutchings and F. Jiao, *J. Am. Chem. Soc.*, 2013, **135**, 4516.
17 P. Shukla, H.Q. Sun, S.B. Wang, H.M. Ang and M.O. Tadé, *Sep. Puri. Technol.*, 2011, **77**, 230.
18 W. Zhang, H.L. Tay, S.S Lim, Y.S. Wang, Z.Y. Zhong and R. Xu, *Appl. Catal. B: Environ.*, 2010, **95**, 93.
19 Z.M. El-Bahy, M.M. Mohamed, F.I. Zidan and M.S. Thabet, *J. Hazard. Mater.*, 2008, **153**, 364.
20 S.J. Lin, G.J. Su, M.H. Zheng, D.K. Ji, M.K. Jia and Y.X. Liu, *Appl. Catal. B: Environ.*, 2012, **123–124**, 440.
21 P.H. Shi, R.J. Su, S.B. Zhu, M.C. Zhu, D.X. Li and S.H. Xu, *J. Hazard. Mater.*, 2012, **229–230**, 331.
22 J.R. Wang and F.E. Osterloh, J. Mater. Chem. A, 2014, **2**, 9405.
23 C.C. Han, L. Ge, C.F. Chen, Y.J. Li, X.L. Xiao, Y.N. Zhang and L.L. Guo, *Appl. Catal. B: Environ.*, 2014, **147**, 546.
24 C.W. Tan, G.Q. Zhu, M. Hojamberdiev, K. Okada, J. Liang, X.C. Luo, P. Liu and Y. Liu, *Appl. Catal. B: Environ.*, 2014, **152–153**, 425.
25 M. C. Long, W. M. Cai, B. X. Zhou, X. Y. Chai and Y. H. Wu, *J. Phys. Chem. B*, 2006, **110**, 20211.
26 H. Y. Zhang, S. Pokhrel, Z. X. Ji, H. Meng, X. Wang, S. J. Lin, C. H. Chang, L. J. Li, R. B. Li, B. B. Sun, M. Y. Wang, Y. P. Liao, R. Liu, T. Xia, L. Mädler and A.E. Nel, *J. Am. Chem. Soc.*, 2014, **136**, 6406.
27 W. L. Yang, L. Zhang, Y. Hu, Y. J. Zhong, H. B. Wu and X. W. Lou, *Angew. Chem. Int. Ed.*, 2012, **51**, 11501.
28 K. Rajeshwar and N. R. Tacconi, Chem. *Soc. Rev.*, 2009, **38**, 1984.
29 F. T. Li, J. R. Ran, M. Jaroniec and S. Z. Qiao, *Nanoscale*, 2015, **7**, 17590.
30 F. T. Li, Q. Wang, J. R. Ran, Y. J. Hao, X. J. Wang, D.S. Zhao and S.Z. Qiao, *Nanoscale*, 2015, **7**, 1116.
31 F. T. Li, Q. Wang, X. J. Wang, B. Li, Y. J. Hao, R. H. Liu and D. S. Zhao, *Appl. Catal. B: Environ.*, 2014, **150–151**, 574.
32 F. T. Li, Y. Liu, ; Z. M. Sun, Y. Zhao, R. H. Liu, L. J. Chen and D. S. Zhao, *Catal. Sci. Technol.*, 2012, **2**, 1455.
33 A. Idris, N. Hassan, R. Rashid and A.F. Ngomsik, *J. Hazard. Mater.*, 2011, **186**, 629.
34 P. Ju, P. Wang, B. Li, H. Fan, S. Y. Ai, D. Zhang and Y. Wang, *Chem. Eng. J.*, 2014, **236**, 430.
35 F. T. Li, Y. Zhao, Q. Wang, X. J. Wang, Y. J. Hao, R. H. Liu and D. S. Zhao, *J. Hazard. Mater.*, 2015, **283**, 371.
36 C. W. Kung, C. Y. Lin, R. Vittal and K. C. Ho, *Sensor. Actuat. B*, 2013, **182**, 429.
37 K. D. Bhatte and B. M. Bhanage, *Mater. Lett.*, 2013, **96**, 60.
38 A. F. Bedilo, M. J. Sigel, O. B. Koper, M. S. Melgunov and K. J. Klabunde, *J. Mater. Chem.*, 2002, **12**, 3599.
39 F. T. Li, Y. Zhao, Y. Liu, Y. J. Hao, R. H. Liu and D. S. Zhao, *Chem. Eng. J.*, 2011, **173**, 750.
40 Z. L. Chen, S. H. Chen, Y. H. Li, X. L. Si, J. Huang, S. Massey and G. L. Chen, *Mater. Res. Bull.*, 2014 , **57**, 170.
41 Y. Y. Lü, W. W. Zhan, Y. He, Y. T. Wang, X. J. Kong, Q. Kuang, Z. X. Xie and L. S. Zheng, *ACS Appl. Mater. Interfaces*, 2014, **6**, 4186.
42 D. Barreca, A. Gasparotto, O. I. Lebedev, C. Maccato, A. Pozza, E. Tondello, S. Turner and G. V. Tendeloo, *CrystEngComm*, 2010, **12**, 2185.
43 C. Fettkenhauer, X. C. Wang, K. Kailasam, M. Antonietti, and D. Dontsova, *J. Mater. Chem. A*, 2015, **3**, 21227.
44 M. A. Garakani, S. Abouali, B. Zhang, C. A. Takagi, Z. L. Xu, J. Q. Huang and J. K. Kim, *ACS Appl. Mater. Interface*s, 2014, **6**, 18971.
45 O. Carp, C. L. Huisman and A. Reller, Prog. *Solid State Chem.*, 2004, **32**, 33.
46 G. A. M. Ali, O. A. Fouad and S. A. Makhlouf, *J. Alloys Comp.*, 2013, **579**, 606.
47 M. Y. Nassar, *Mater. Lett.*, 2013, **94**, 112.
48 X. F. Huang, T. C. Cao, M. C. Liu and G. H. Zhao, *J. Phys. Chem. C*, 2013, **117**, 26432.
49 P. Raja, M. Bensimon, U. Klehm, P. Albers, D. Laub, L. Kiwi-Minsker, A. Renken and J. Kiwi, *J. Photochem. Photobio. A: Chem*., 2007, **187**, 332.
50 O. Akdim, U. B. Demirci and P. Miele, *Intern. J. Hydrogen Energy*, 2009, **34**, 9444.
51 F. Li, E. E. Arthur, D. La, Q. M. Li and H. Kim, *Energy*, 2014, **71**, 32.
52 M. Abdullah, G. K. C. Low and R. W. Matthews, *J. Phys. Chem.*, 1990, **94**, 6820.
53 E. Jimenez-Relinque and M. Castellote, *Cem. Concr. Res.*, 2015, **74**, 108.
54 A. Fujishima and X. T. Zhang, *C. R. Chimie*, 2006, **9**, 750.
55 S. Kim and W. Choi, *Environ. Sci. Technol*. 2002, **36**, 2019.

$CoCl_2 \cdot 6H_2O$ is introduced into $Co_3O_4$ for the in-situ enhancement of hydroxyl radicals and the construction of heterojunctions

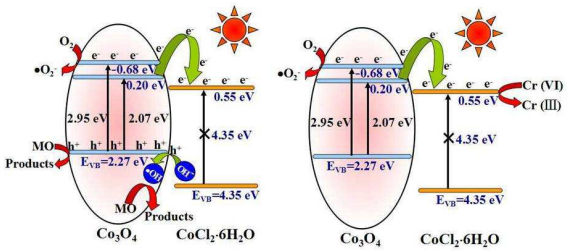


Oxidation of methyl orange (MO) Reduction of Cr(VI)